JGR Oceans

RESEARCH ARTICLE
10.1029/2021JC018102

Resolution Dependence of Atmosphere–Ocean Interactions and Water Mass Transformation in the North Atlantic

Dylan Oldenburg[1], Robert C. J. Wills[2], Kyle C. Armour[1,2], and LuAnne Thompson[1]

[1]School of Oceanography, University of Washington, Seattle, WA, USA, [2]Department of Atmospheric Sciences, University of Washington, Seattle, WA, USA

Key Points:

- A high-resolution coupled simulation skillfully reproduces climatological water mass transformation in the subpolar North Atlantic
- Despite climatological differences between low- and high-resolution models, the Labrador Sea plays a major role in AMOC variability in both
- High-resolution simulations show a larger atmospheric response to low-frequency AMOC variability

Supporting Information:

Supporting Information may be found in the online version of this article.

Correspondence to:

D. Oldenburg,
oldend@uw.edu

Citation:

Oldenburg, D., Wills, R. C. J., Armour, K. C., & Thompson, L. (2022). Resolution dependence of atmosphere–ocean interactions and water mass transformation in the North Atlantic. *Journal of Geophysical Research: Oceans*, *127*, e2021JC018102. https://doi.org/10.1029/2021JC018102

Received 7 OCT 2021
Accepted 21 MAR 2022

Abstract Water mass transformation (WMT) in the North Atlantic plays a key role in driving the Atlantic Meridional Overturning Circulation (AMOC) and its variability. Here, we analyze subpolar North Atlantic WMT in high- and low-resolution versions of the Community Earth System Model version 1 (CESM1) and investigate whether differences in resolution and climatological WMT impact low-frequency AMOC variability and the atmospheric response to this variability. We find that high-resolution simulations reproduce the WMT found in a reanalysis-forced high-resolution ocean simulation more accurately than low-resolution simulations. We also find that the low-resolution simulations, including one forced with the same atmospheric reanalysis data, have larger biases in surface heat fluxes, sea-surface temperatures, and salinities compared to the high-resolution simulations. Despite these major climatological differences, the mechanisms of low-frequency AMOC variability are similar in the high- and low-resolution versions of CESM1. The Labrador Sea WMT plays a major role in driving AMOC variability, and a similar North Atlantic Oscillation-like sea-level pressure pattern leads AMOC changes. However, the high-resolution simulation shows a pronounced atmospheric response to the AMOC variability not found in the low-resolution version. The consistent role of Labrador Sea WMT in low-frequency AMOC variability across high- and low-resolution coupled simulations, including a simulation which accurately reproduces the WMT found in an atmospheric-reanalysis-forced high-resolution ocean simulation, suggests that the mechanisms may be similar in nature.

Plain Language Summary Water mass transformation, which is a measure of density change in the surface ocean, plays an important role in variations in the Atlantic Meridional Overturning Circulation (AMOC). Here, we use high- and low-resolution-coupled model simulations to determine whether resolution and time-mean water mass transformation patterns impact AMOC variations. We find that a high-resolution coupled simulation reproduces the water mass transformation from our closest analog to observations and yields more realistic surface ocean features than its low-resolution counterpart. Despite these differences, the mechanisms governing decadal and multidecadal AMOC variations are similar in the two simulations. In both simulations, the Labrador Sea plays a prominent role in driving decadal and multidecadal AMOC variations. Given that the high-resolution simulation accurately reproduces the water mass transformation patterns found in our closest analog to observations, it is likely that the Labrador Sea plays a major role in driving AMOC variations in nature as well.

1. Introduction

The Atlantic Meridional Overturning Circulation (AMOC) plays a key role in global climate by transporting large amounts of heat northward into the high latitudes. The North Atlantic Current, which forms the upper branch of AMOC, carries warm, salty subtropical water northward into the subpolar regions, releasing large amounts of heat to the atmosphere. The heat exchange with the atmosphere transforms the water into cooler, denser Subpolar Mode Water (Brambilla & Talley, 2008; McCartney & Talley, 1982; Pérez-Brunius et al., 2004). This process of converting water parcels from one density class to another is referred to as water mass transformation (WMT).

AMOC exhibits substantial low-frequency variability in global climate models (e.g., Delworth & Zeng, 2016; Kwon & Frankignoul, 2014; MacMartin et al., 2016), which leads to substantial variations in both North Atlantic and Arctic climate (e.g., Covey & Thompson, 1989; Day et al., 2012; Oldenburg et al., 2018; Zhang, 2015). Low-frequency AMOC variability is associated with variations in the upper ocean density in the northern subpolar gyre (Roberts et al., 2013; Robson et al., 2016) as well as North Atlantic sea-level pressure (SLP) patterns

associated with changes in the North Atlantic Oscillation (NAO; Delworth & Zeng, 2016; Delworth et al., 2016; Eden & Jung, 2001; Kim et al., 2018, 2020; Mecking et al., 2015).

AMOC is closely linked to the subpolar North Atlantic WMT (Grist et al., 2009; Isachsen et al., 2007; Josey et al., 2009; Langehaug, Rhines, et al., 2012; Marsh, 2000), which is responsible for driving high-latitude deep water formation. The link between WMT and AMOC has been the subject of many studies, mainly using low-resolution (∼1°) global climate models (e.g., Langehaug, Rhines, et al., 2012). However, low-resolution global climate models vary in their representation of which deep water formation regions dominate the AMOC structure and variability (e.g., Heuze, 2017; Langehaug, Rhines, et al., 2012; Menary et al., 2015; Oldenburg et al., 2021). The biases in the deep water formation regions coincide with biases in subpolar temperature and salinity relative to observations (Langehaug, Rhines, et al., 2012). In addition, Nordic Seas overflow processes, which are responsible for producing the dense water masses that make up the southward flowing branch of AMOC and take place at comparatively small spatial scales (Langehaug, Medhaug, et al., 2012; Treguier et al., 2005), tend to be weak in low-resolution ocean models compared to observations (Bailey et al., 2005). This results in a deficit in the volume transport of these water masses. Moreover, low-resolution models do not resolve ocean mesoscale eddies, which are known to contribute to WMT via convection and lateral buoyancy fluxes, particularly in the Labrador Sea (Garcia-Quintana et al., 2019).

Previous work using low-resolution model simulations shows that low-frequency AMOC variability is associated with large changes in Labrador Sea WMT regardless of where the climatological WMT is concentrated (Oldenburg et al., 2021). The mechanism of low-frequency AMOC variability involves upper ocean cooling and densification in the Labrador Sea, driven by northwesterly winds off eastern North America. This increases deep water formation there, which later strengthens AMOC. The strengthened AMOC carries anomalous warm water northward into the subpolar regions, weakening deep water formation and hence AMOC. This mechanism, dominated by Labrador Sea WMT variability, holds true across a range of low-resolution models with distinct representations of deep water formation in subpolar regions (Oldenburg et al., 2021). However, one concern with these results is that low-resolution simulations likely overestimate deep water formation and subduction in the Labrador Sea region compared to high-resolution ocean simulations (Garcia-Quintana et al., 2019). This is because of the large role that convective eddies play during the restratification phase in the spring and summer months. Mixed-layer depths are also likely too deep in low-resolution models owing to the absence of eddies (Garcia-Quintana et al., 2019).

Low-resolution models also tend to underestimate the atmospheric responses to AMOC and sea-surface temperature (SST) variability relative to observations and high-resolution models (Czaja et al., 2019). While various observational and reanalysis-based studies have found substantial NAO-like responses to decadal and multidecadal SST changes (e.g., Czaja & Frankignoul, 1999, 2002; Czaja et al., 2019; Gastineau & Frankignoul, 2015; Venzke et al., 1999; S. M. Wills et al., 2016), several low-resolution models show no discernible atmospheric response to SST variations associated with AMOC variability (Oldenburg et al., 2021).

This previous work raises several interesting questions related to the resolution dependence of North Atlantic atmosphere–ocean interactions, WMT, and AMOC variability. (a) Do the mechanisms of low-frequency AMOC and northward ocean heat transport (OHT) variability found in low-resolution models, where the Labrador Sea appears to be the most important region for initiating AMOC variability (Oldenburg et al., 2021), still hold in high-resolution models? (b) How does the ocean resolution of a model affect the partitioning of WMT between the different deep water formation regions? (c) Finally, do high-resolution model simulations show evidence of a stronger NAO response to AMOC, as suggested by observations?

In this paper, we will investigate these questions using high- and low-resolution versions of Community Earth System Model version 1 (CESM1). We evaluate how well a high-resolution-coupled simulation reproduces the surface-forced WMT found in a high-resolution atmospheric-reanalysis-forced ocean simulation, which we consider as an analog to observations, and compare that to what is found in a low-resolution simulation. We then analyze the factors that set the magnitude of WMT in these simulations and examine the mechanisms of low-frequency AMOC variability in the high- and low-resolution versions of the coupled model. We focus in particular on the link between the AMOC variability and the WMT variability in the different deep water formation regions and on how the variability is affected by the differences in resolution and mean state. Finally, we investigate the atmospheric response to the AMOC variability in the two simulations.

In Section 2, we describe the model simulations used in this analysis. In Section 3, we compute the WMT and AMOC in the different simulations and analyze the factors that explain the differences between them. In Section 4, following the methods of Oldenburg et al. (2021), we use a low-frequency component analysis (LFCA) to elucidate the mechanisms of low-frequency AMOC variability in the high- and low-resolution versions of the coupled model and investigate the atmospheric response to the AMOC variability in these models. In Section 5, we summarize and discuss the overall results and conclusions.

2. Description of Models

We use output from a 1,800-year preindustrial control simulation of the CESM1.1 (Hurrell, 2013), with a nominal horizontal resolution of 1° in the atmosphere and ocean. We henceforth refer to this low-resolution CESM1 simulation as CESM1-LR. We also use output from a 500-year preindustrial control simulation of CESM1.3 by the International Laboratory for High-Resolution Earth System Prediction (iHESP; Chang et al., 2020), which uses an eddy-resolving 0.1° version of the Parallel Ocean Component version 2 (POP2) and a 0.25° version of the Community Atmosphere Model version 5 (CAM5). We henceforth refer to this high-resolution CESM1 simulation as CESM1-HR. Unlike its low-resolution counterpart, this model does not include a parameterization for overflows of deep water from the Nordic Seas into the North Atlantic while still not fully resolving the overflow processes. Here, we analyze the last 350 years of the 500-year simulation, because the first 150 years are considered spin-up, during which the upper ocean experiences rapid adjustment. Given that this spin-up period is fairly short, the deep ocean state continues to drift throughout the simulation.

For our analysis of reanalysis-forced ocean–sea-ice simulations, we use output from 1° and 0.1° POP2 ocean simulations (Kim et al., 2021), which are both forced with atmospheric reanalysis data from the Japanese 55-year Reanalysis (JRA55, Harada et al., 2016; Kobayashi et al., 2015), spanning years 1958–2018. Henceforth, we refer to these low- and high-resolution simulations as JRA55-LR and JRA55-HR, respectively. Here, we are seeking an analog to observations which still provides full ocean output data. Given that historical ocean observations are limited to particular regions or require reconstruction from proxies, an atmospheric-reanalysis-forced ocean simulation, which includes an ocean constrained at the surface to best estimates of historical atmospheric states, is a useful alternative. It would be possible to instead use ocean assimilation data. However, they typically do not have closed heat and salt budgets, which are important when linking WMT to the interior ocean state. Also, historical ocean observations are fairly limited compared to atmospheric observational data, which reduces the reliability of assimilation products. Hence, we take JRA55-HR as our closest analog to observations.

Differences in initialization between simulations could lead to differences in their climatologies, so we briefly discuss how each simulation was spun up. CESM1-LR's ocean was initialized from January-mean present-day potential temperature from PHC2, and its atmosphere, land, and sea ice were initialized from a previous CESM1 (CAM5) 1850 control run. The ocean component of CESM1-LR was initialized with January-mean potential temperature and salinity from World Ocean Atlas 2013 data (Locarnini et al., 2013; Zweng et al., 2013) from a state of rest, and the initial conditions for the other components were taken from restart files of previous simulations. Both JRA55 simulations were initialized from rest using temperatures and salinities from the World Ocean Atlas. The low-resolution version was spun up over five cycles, and the high resolution had no spin-up period prior to the simulation. Sea-surface salinities were restored via a salinity-restoring flux. The sensible and latent heat fluxes were calculated based on the SSTs and the JRA55 air temperatures during runtime, resulting in SSTs that closely resemble the JRA55 surface air temperatures (Chassignet et al., 2020).

We compare the rest of the simulations to JRA55-HR to determine whether increasing the ocean and atmospheric resolution of a coupled model leads to a more accurate representation of WMT and AMOC. Comparing JRA55-LR with CESM1-LR illustrates the role of atmospheric forcing (reanalysis data vs. a coupled atmosphere) at the same ocean model resolution, while comparing JRA55-LR with JRA55-HR illustrates the role of ocean model resolution (parameterized vs. resolved mesoscale eddies) under the same atmospheric forcing.

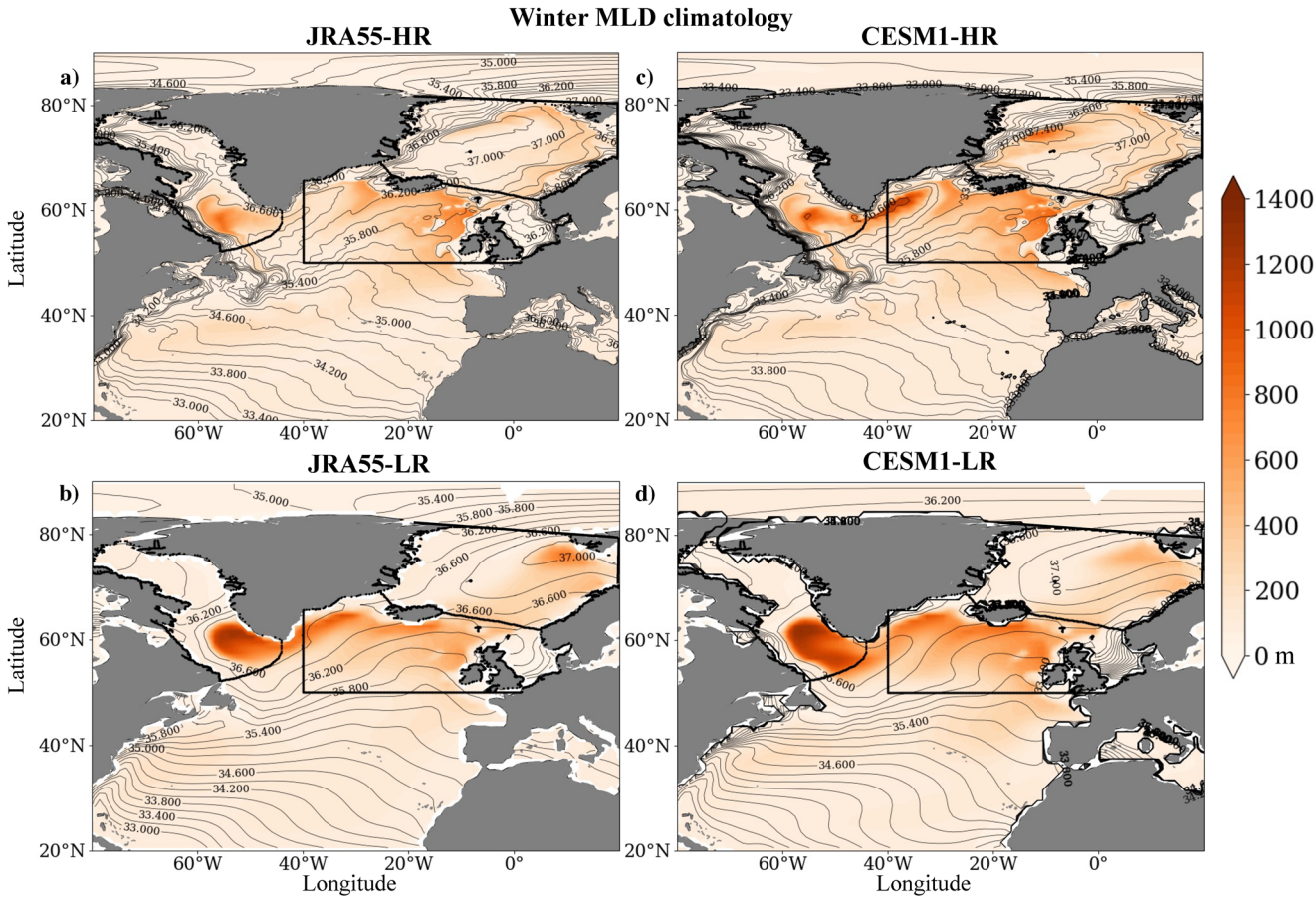

Figure 1. Climatological mixed-layer depth (colors) and sea-surface potential density referenced to 2,000 m (contours) both averaged over January–March in (a) JRA55-HR, (b) JRA55-LR, (c) CESM1-HR, and (d) CESM1-LR. The thick black lines represent the region masks for the Labrador Sea (left), Irminger–Iceland Basins (lower right), and Greenland–Iceland–Norwegian (GIN) Seas (upper right).

3. Comparison of WMT and AMOC Climatologies

Before analyzing WMT and AMOC, it is helpful to consider the time-mean winter (January–March) mixed-layer depth to determine where the deep convection and deep water formation occur in the different models. In JRA55-HR, deep mixed layers are concentrated mostly in the Labrador Sea and Irminger–Iceland Basins (IIBs), with some deep mixed layers in the Greenland–Iceland–Norwegian (GIN) Seas as well (Figure 1a). In JRA55-LR, the mixed layers overall are deeper, and the deepest mixed layers are concentrated in the Labrador Sea, though there are still deep mixed layers in the IIB and GIN Seas (Figure 1b). In CESM1-HR, the mixed-layer depth patterns look similar to JRA55-HR, but the mixed-layer depths are deeper in all of the deep water formation regions (Figure 1c). In CESM1-LR, the deepest mixed layers are mostly concentrated in the Labrador Sea, even more so than in JRA55-LR, which shows similar overall patterns (Figures 1b and 1d). It is noteworthy that CESM1-HR captures the mixed-layer depth patterns found in JRA55-HR much better than either of the low-resolution models, despite JRA55-LR being forced with the same atmospheric reanalysis data as JRA55-HR.

To investigate differences in AMOC and its variability across these simulations, we use AMOC calculated in density coordinates rather than AMOC calculated in depth coordinates, because it is more appropriate for analyzing subpolar AMOC variability and is strongly connected to the analysis of WMT as a function of density class (Pickart & Spall, 2007; Straneo, 2006). We first look at the AMOC climatology to determine how well the coupled simulations (and JRA55-LR) reproduce the AMOC from the reanalysis-forced high-resolution data set, JRA55-HR. To compute AMOC, we use the following equation from Newsom et al. (2016):

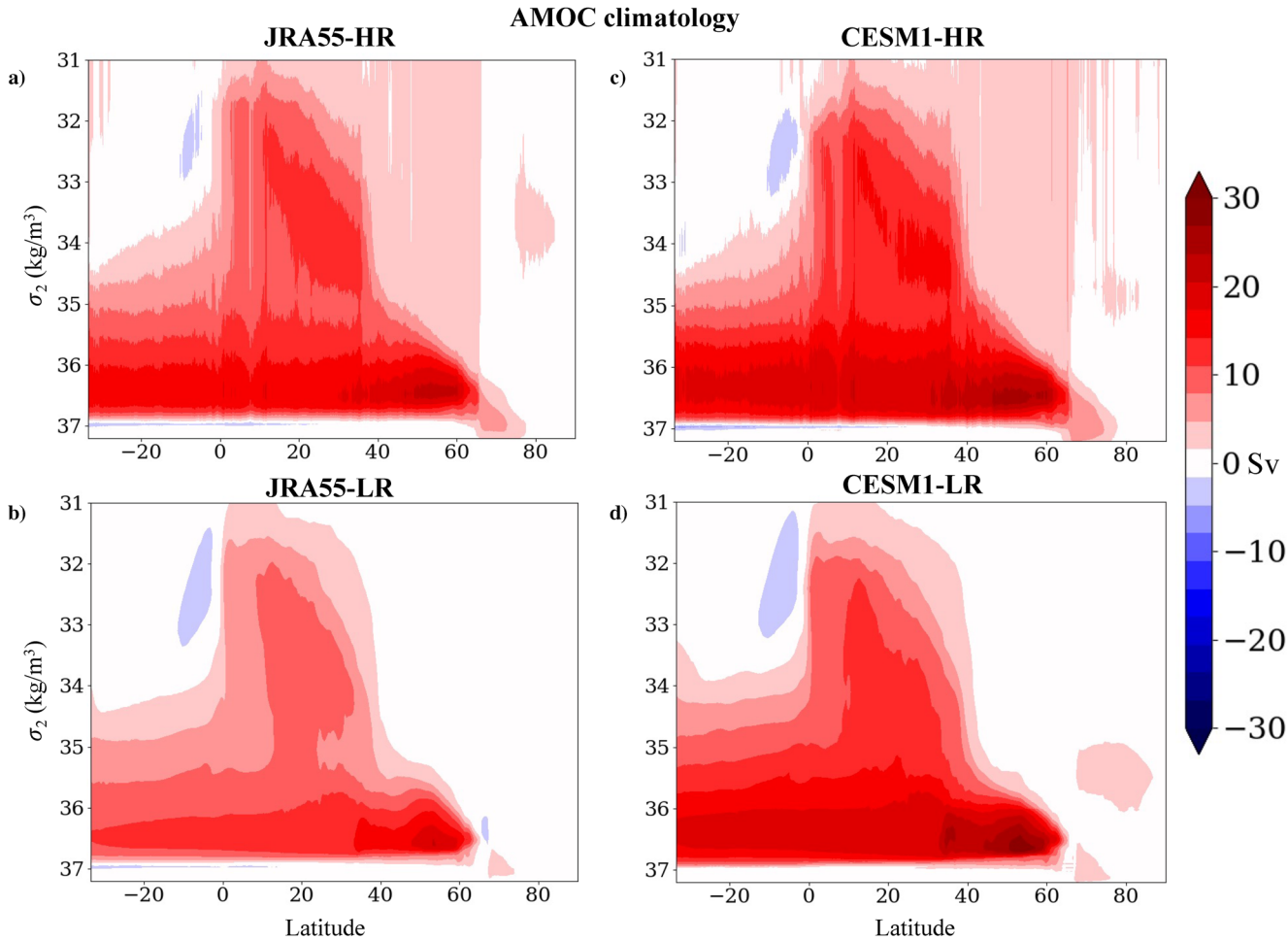

Figure 2. Climatological Atlantic Meridional Overturning Circulation (AMOC) in (a) JRA55-HR, (b) JRA55-LR, (c) CESM1-HR and (d) CESM1-LR.

$$\mathrm{AMOC}(\sigma, y, t) = -\int_{x_W}^{x_E} \int_{-B(x,y)}^{z(x,y,\sigma,t)} v(x, y, z, t)\, dz\, dx, \tag{1}$$

where σ is the potential density referenced to 2,000 m, y is the latitude, x is longitude, x_W and x_E are the western and eastern longitudinal limits of the basin, respectively, v is the meridional velocity, z is depth (positive upward), $B(x, y)$ is the bottom depth, and t is time.

In JRA55-HR, the maximum AMOC is located at $\sigma_2 = 36.48$ kg m^{-3}, where it reaches 21.8 Sv (Figure 2a). In JRA55-LR, the maximum is located at $\sigma_2 = 36.58$ kg m^{-3} and is equal to 20.7 Sv (Figure 2b). AMOC in CESM1-HR reaches a maximum of 25.4 Sv at $\sigma_2 = 36.53$ kg m^{-3} (Figure 2c). In CESM1-LR, AMOC reaches a maximum of 28.6 Sv at $\sigma_2 = 36.64$ kg m^{-3} (Figure 2d). Hence, in terms of maximum magnitude, JRA55-LR reproduces the AMOC found in JRA55-HR the best of all the other model simulations, though CESM1-HR reproduces the density where the maximum occurs most accurately. Surprisingly, the maximum AMOC is actually smaller in JRA55-LR than in JRA55-HR; we would expect a higher-resolution simulation to yield a weaker AMOC given the reduced Labrador Sea deep water formation, as in CESM1-HR and CESM1-LR, and also what was found in other studies of coupled GCMs (Sein et al., 2018; Winton et al., 2014). All of the simulations have AMOC maxima located at higher densities than JRA55-HR. CESM1-HR has a maximum AMOC at a density closest to the JRA55-HR maximum, while CESM1-LR has a maximum AMOC at a density furthest from the JRA55-HR maximum. These results indicate that although increasing the resolution of the atmosphere and ocean yields an AMOC substantially closer in structure and magnitude to reanalysis-forced ocean data, there are likely

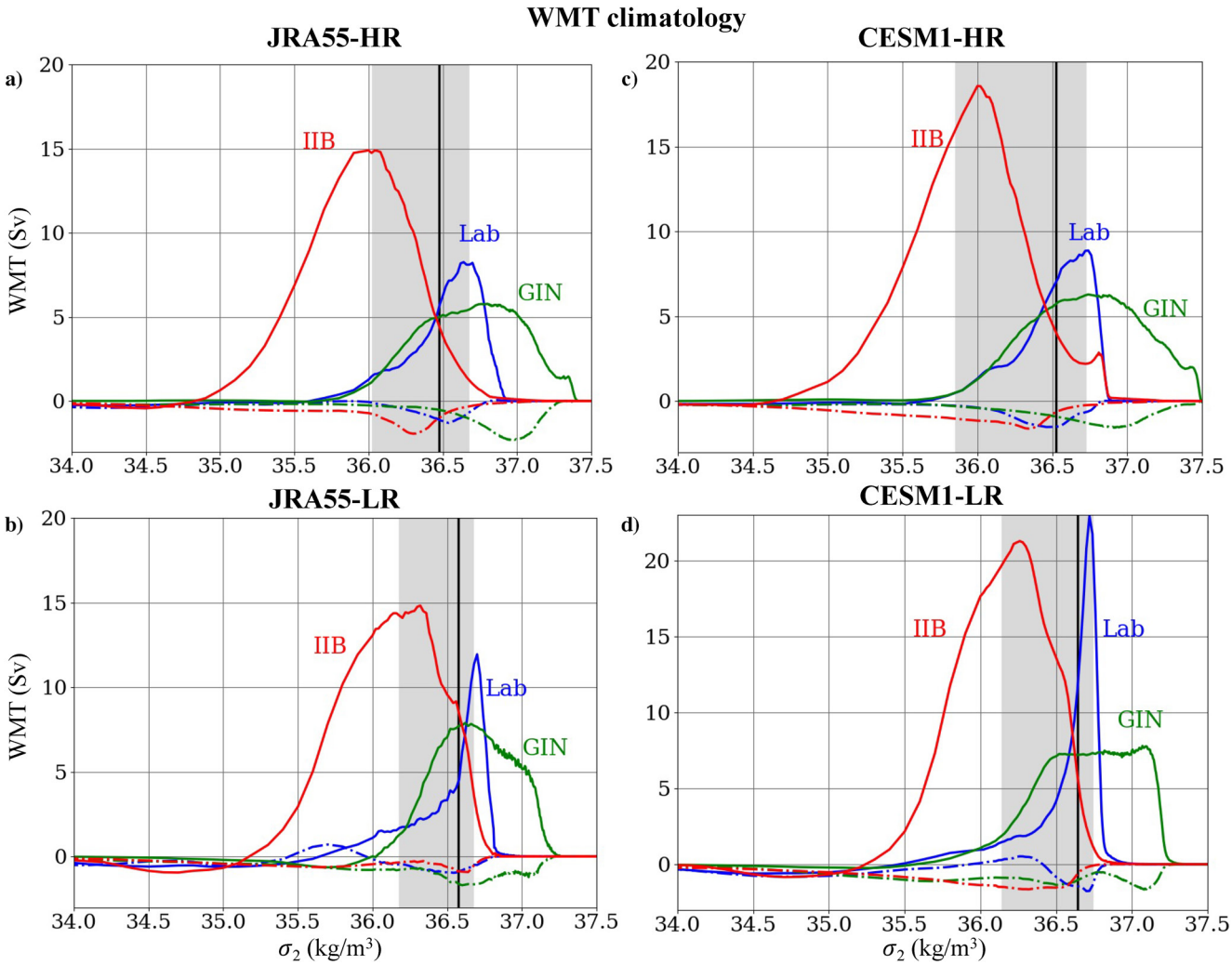

Figure 3. Climatological water mass transformation thermal (solid lines) and freshwater (dashed lines) components in the Labrador Sea (Lab), GIN Seas, and IIB for (a) JRA55-HR, (b) JRA55-LR, (c) CESM1-HR, and (d) CESM1-LR. The black vertical lines indicate the density where the climatological AMOC reaches its maximum in each model. The gray shaded areas represent the density range where AMOC is within 25% of its maximum value. A more detailed illustration of what particular areas of the deep water formation regions contribute to the surface-density flux over different density classes is shown in Figures 4 and 5, as well as Figure S1 in Supporting Information S1. Note the difference in scale between (d) and the other panels.

biases in the atmospheric component of the coupled simulations even at high resolution. These differences in AMOC structure may also to some extent stem from the fact that these simulations were run with distinct initial conditions and had different spin-up procedures.

To compute the surface-forced WMT, we follow the methodology used in Oldenburg et al. (2021) among others. Here, as in Oldenburg et al. (2021), we neglect the mixing contributions because the time resolution of the model output data is not high enough to calculate them. We compute the WMT separately in the Labrador Sea, IIB, and GIN Seas using the region masks shown in the boxes in Figure 1 to determine each region's contribution to the total WMT.

In all four simulations, the thermal WMT component dominates over the haline contribution. However, the partitioning of total WMT in the different regions varies substantially among the simulations. In JRA55-HR, none of the peaks in WMT in the different regions align with the density of maximum AMOC, likely due to the absence of the effects of mixing in this calculation. The IIB contributes the most to the WMT at densities lower than the density of maximum AMOC (Figure 3a), reaching a maximum value of 14.2 Sv at $\sigma_2 = 36$ kg m^{-3}. At densities higher than the maximum AMOC, the WMT is dominated by contributions from the Labrador Sea and GIN Seas,

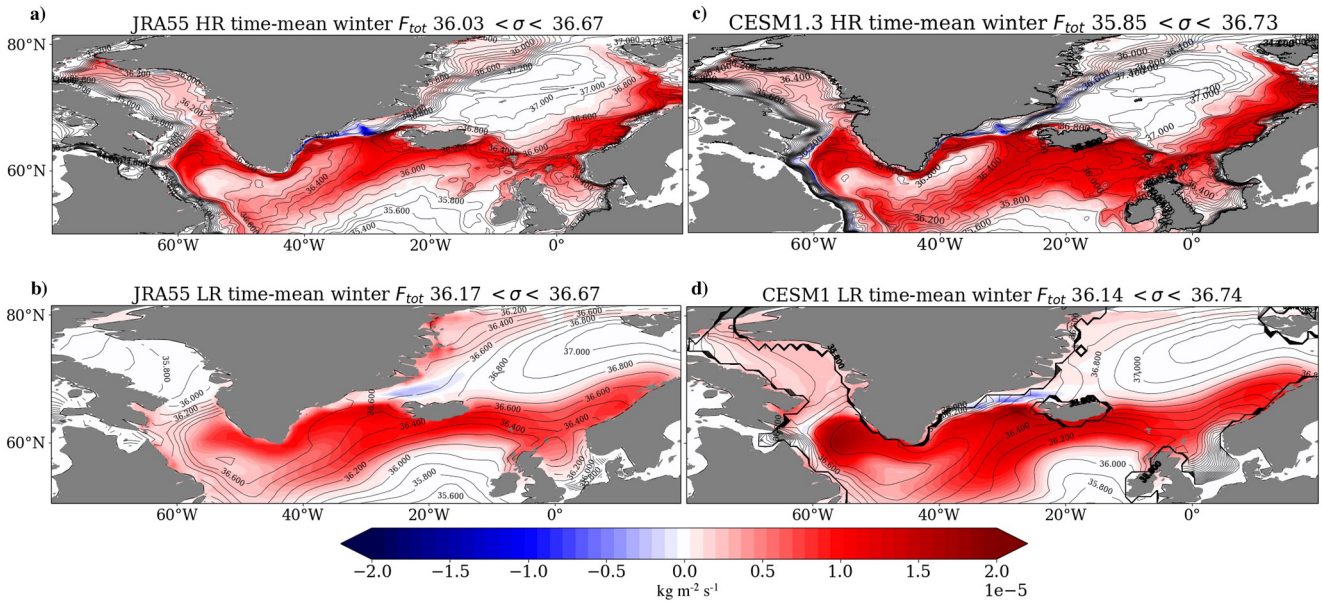

Figure 4. Colors: Total climatological winter surface-density flux calculated using the methodology from Oldenburg et al. (2021) over densities where AMOC is at least 75% of its maximum. Contours: Time-mean winter sea-surface potential density referenced to 2,000 m for (a) JRA55-HR, (b) JRA55-LR, (c) CESM1-HR, and (d) CESM1-LR.

with a much narrower peak in the Labrador Sea. The Labrador Sea has a peak of 7.7 Sv at $\sigma_2 = 36.7$ kg m^{-3}, and the GIN Seas WMT peaks at 4.6 Sv at $\sigma_2 = 36.56$ kg m^{-3}. Though these densities are further away from the maximum AMOC, they are likely still important for AMOC given that internal mixing acts to reduce the density of the densest water masses. In JRA55-LR, the peaks in the IIB and GIN Seas WMT occur closer to the maximum AMOC than in JRA55-HR, reaching maxima equal to 14.5 and 6.2 Sv at $\sigma_2 = 36.32$ and $\sigma_2 = 36.62$, respectively, and the IIB dominates the WMT near the AMOC maximum (Figure 3b). The Labrador Sea peak in WMT is located at about the same density as in JRA55-HR, with a peak value of 11.4 Sv at $\sigma_2 = 36.7$ kg m^3. Furthermore, the peaks in the Labrador Sea and GIN Seas WMT are narrower in JRA55-LR than they are in JRA55-HR.

The WMT in CESM1-HR looks the most similar to JRA55-HR of all the other simulations, with the most notable difference being that the WMT peaks in the IIB and Labrador Sea WMT are larger than in JRA55-HR (Figure 3c), with the IIB WMT reaching a maximum value of 17.4 Sv at $\sigma_2 = 36$ kg m^{-3}, the Labrador Sea WMT reaching a maximum of 8.3 Sv at $\sigma_2 = 36.74$ kg m^{-3}, and the GIN Seas WMT peaking at 5.0 Sv at $\sigma_2 = 36.74$ kg m^{-3}. However, the partitioning of the WMT between the different regions remains similar to JRA55-HR. In CESM1-LR, on the other hand, the WMT looks quite different, with much larger WMT peaks in the IIB and the Labrador Sea WMT than in any of the other simulations (Figure 3d), reaching maxima equal to 19.6 and 21.2 Sv at $\sigma_2 = 36.26$ and $\sigma_2 = 36.72$, respectively. The peak in Labrador Sea WMT is also much narrower than in JRA55-HR and CESM1-HR and looks more similar to JRA55-LR. The GIN Seas WMT peaks at $\sigma_2 = 36.82$ kg m^{-3}, where it reaches a maximum of 6.9 Sv. This seems to indicate that increasing the atmospheric and ocean resolution in a coupled model yields a fairly realistic representation of WMT in the different deep water formation regions, certainly much more realistic than an equivalent low-resolution-coupled model. The substantial discrepancies between JRA55-LR and JRA55-HR indicate that a higher ocean model resolution provides a more accurate representation of WMT and AMOC beyond what is provided by simply having correct atmospheric surface forcing.

To illustrate which parts of each region contribute to the WMT in different density classes, it is useful to look at the full surface-density flux calculated using the methodology of Oldenburg et al. (2021) and others. Since we are interested in the density classes relevant for AMOC, we isolate the density flux for densities lower than the minimum density where AMOC reaches 75% of its maximum value (Figure S1 in Supporting Information S1), densities within the density range where AMOC is at least 75% of its maximum value (Figure 4), and densities beyond that density range (Figure 5). In the lowest density range, the surface-density flux is concentrated in the

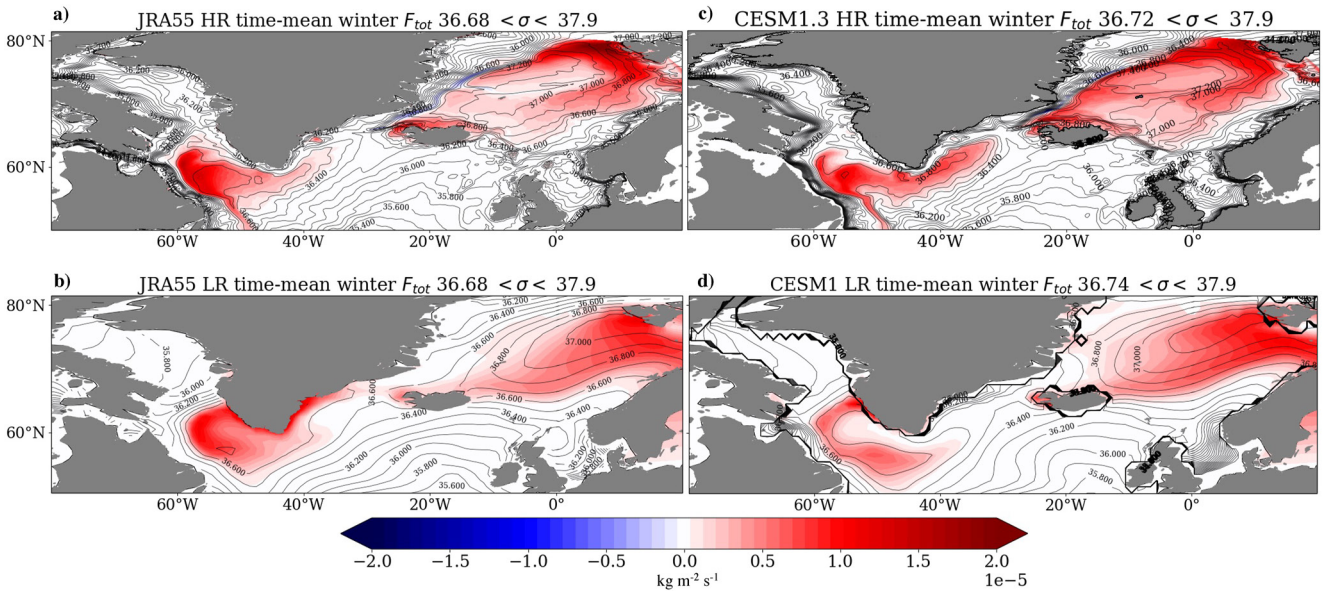

Figure 5. Colors: Total climatological winter surface-density flux calculated using the methodology from Oldenburg et al. (2021) over densities above the maximum density where AMOC reaches 75% of its maximum. Contours: Time-mean winter sea-surface potential density referenced to 2,000 m for (a) JRA55-HR, (b) JRA55-LR, (c) CESM1-HR, and (d) CESM1-LR.

IIB, with small contributions from the other regions, mainly near coastlines where the water is fresher and lighter than the interior areas (Figure S1 in Supporting Information S1). Because interior mixing tends to reduce the density of water parcels, the surface-density fluxes in this density range are unlikely to contribute to AMOC.

In the density range near the AMOC maximum, CESM1-HR reproduces the density flux patterns found in JRA55-HR fairly well. In both of these simulations, most of the Labrador Sea surface-density flux is concentrated in the northern section of the Labrador Sea rather than in the southern section, where density fluxes are weaker (Figures 4a and 4c). The patterns found in the GIN Seas are also similar; however, the surface-density fluxes in the southern part of the IIB are much higher in CESM1-HR than in JRA55-HR (Figures 4a and 4c). The low-resolution simulations show similar overall patterns to JRA55-HR, but lack several key features (Figures 4b and 4d). For example, Labrador Sea fluxes are more concentrated in the central and southern sections compared to JRA55-HR and CESM1-HR, particularly in CESM1-LR (Figure 4d). JRA55-LR reproduces the flux patterns in the IIB fairly well (Figure 4b). However, neither low-resolution simulation has an accurate representation of the more complex smaller scale density structures found in JRA55-HR and CESM1-HR, where the densities are less uniform, particularly near coastlines. For the highest density range, the interior and southern parts of the Labrador Sea contribute more to WMT in JRA55-HR and CESM1-HR compared to the lower density classes (Figures 5a and 5c). There are also larger contributions from the interior and northern parts of the GIN Seas. The same overall patterns are found in the low-resolution simulations (Figures 5b and 5d). However, in JRA55-LR, the surface-density fluxes in the Labrador Sea are shifted to the east relative to JRA55-HR and CESM1-HR, and the northern part of the GIN Seas is not emphasized as much as in the high-resolution simulations, with a much more uniform pattern in the eastern GIN Seas (Figure 5b). In CESM1-LR, the contributions to WMT from the Labrador Sea are smaller, and the eastern area of the GIN Seas is more emphasized compared to in JRA55-LR (Figure 5d).

To allow for a more direct comparison between AMOC and the WMT in the different regions, we also calculate the surface-forced overturning stream function following the methodology of Marsh (2000), Oldenburg et al. (2021), and others. We calculate the surface-forced overturning stream function for each of the three regions separately, which allows us to quantify how much the surface-forced WMT in each region contributes to AMOC (neglecting mixing). CESM1-HR reproduces the surface-forced overturning found in JRA55-HR far better than either low-resolution simulation in all regions (Figures 6a–6d and 6). In JRA55-LR and CESM1-LR, the overturning is too strong in all the regions, especially in the Labrador Sea and IIB (Figures 6e–6h and 6). Also, the

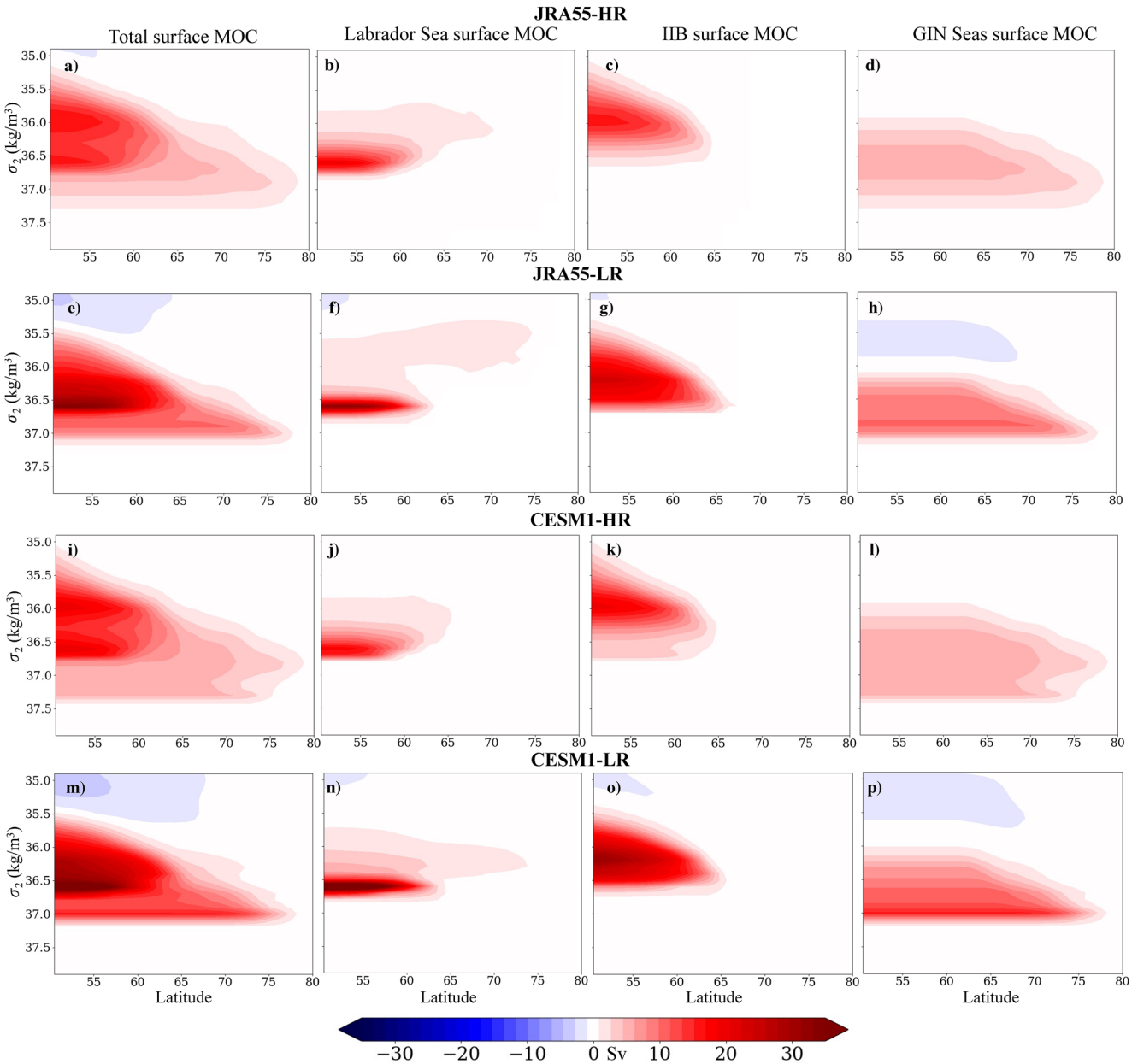

Figure 6. Climatological surface-forced overturning stream function in (a–d) JRA55-HR, (e–h) JRA55-LR, (i–l) CESM1-HR, and (m–p) CESM1-LR computed over all regions (first column), the Labrador Sea (second column), the Irminger–Iceland Basins (IIBs, third column), and GIN Seas (fourth column).

Labrador Sea surface-forced overturning is concentrated over a smaller density range in the LR models compared to the HR versions (Figures 6b, 6f, 6j and 6n). For the IIB, overturning in the HR simulations is shifted toward lower densities compared to the LR versions (Figures 6c, 6g, 6k and 6o). Overturning in the GIN Seas is also concentrated over a smaller density range in the LR models than in the HR models (Figures 6d, 6h, 6l and 6p).

To determine what is responsible for the discrepancies in the WMT between JRA55-HR and the other simulations, we discuss the climatologies of several surface properties used in the WMT calculation, including the sea-surface heat fluxes as well as the sea-surface potential temperatures, salinities, and densities. Although the freshwater fluxes also contribute to the WMT, the freshwater components of WMT are very small in all four simulations (Figure 3). Hence, we do not show them here, but rather in the supplementary section (Figure S2 in Supporting Information S1). Here, we present each quantity in JRA55-HR (Figures 7a and 7e) and the anomalies for the

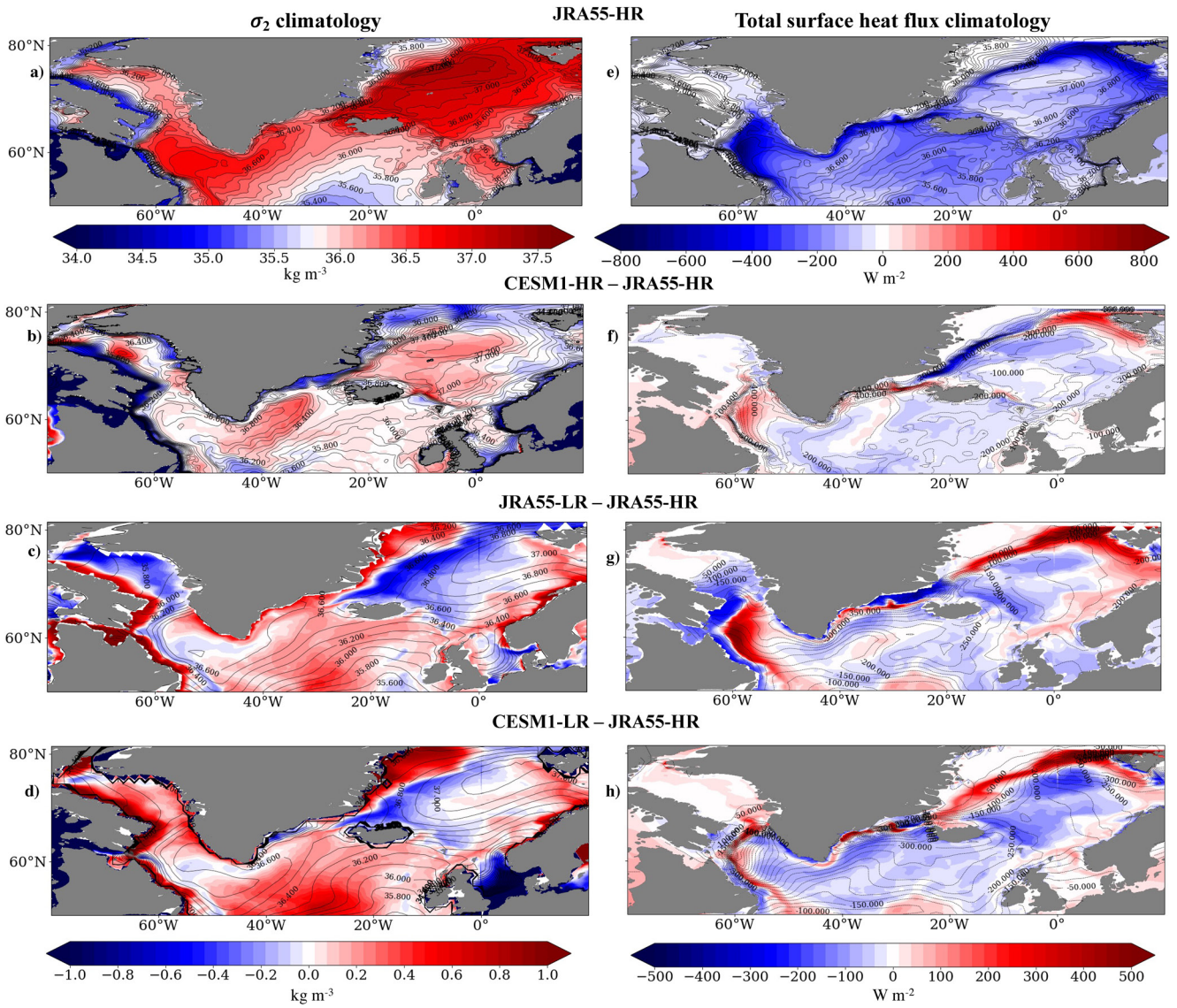

Figure 7. (a) JRA55-HR climatology of sea-surface potential density, referenced to 2,000 m. (b–d) Sea-surface potential density climatologies (contours) and anomalies relative to JRA55-HR (colors) for (b) CESM1-HR, (c) JRA55-LR, and (d) CESM1-LR. (e) JRA55-HR total sea-surface heat flux climatology. (f–h) Sea-surface heat flux climatologies (contours) and anomalies relative to JRA55-HR (colors) for (f) CESM1-HR, (g) JRA55-LR, and (h) CESM1-LR.

other simulations relative to JRA55-HR. CESM1-HR shows a much more accurate representation of the time-mean density structure compared to both low-resolution simulations, particularly in the Labrador Sea and near all coastlines (Figure 7b). CESM1-HR anomalies in SSTs and salinities relative to JRA55-HR are more substantial than its density anomalies (Figures 8b and 8f), but they are mostly density compensating, yielding smaller density anomalies. These anomalies lead to small positive density anomalies in the GIN Seas, IIB, and Labrador Sea, except near the coastlines (Figure 7b), likely due to increased freshwater runoff compared to JRA55-HR (Figure S2 in Supporting Information S1). JRA55-LR, on the other hand, shows large negative density anomalies in the central GIN Seas, but positive anomalies near the coastlines (Figure 7c). There are also positive anomalies in the eastern subpolar gyre and in the northern Labrador Sea. The density structure looks similar in CESM1-LR, with similar anomalies relative to JRA55-HR in most regions, except for in the northern Labrador Sea where there are actually positive anomalies (Figure 7c), due to a fairly salty Labrador Sea compared to the other simulations (Figure 8g). The higher densities in the low-resolution simulations explain why the WMT and AMOC peaks occur at higher densities than in JRA55-HR and CESM1-HR (Figure 3), and the generally more uniform density

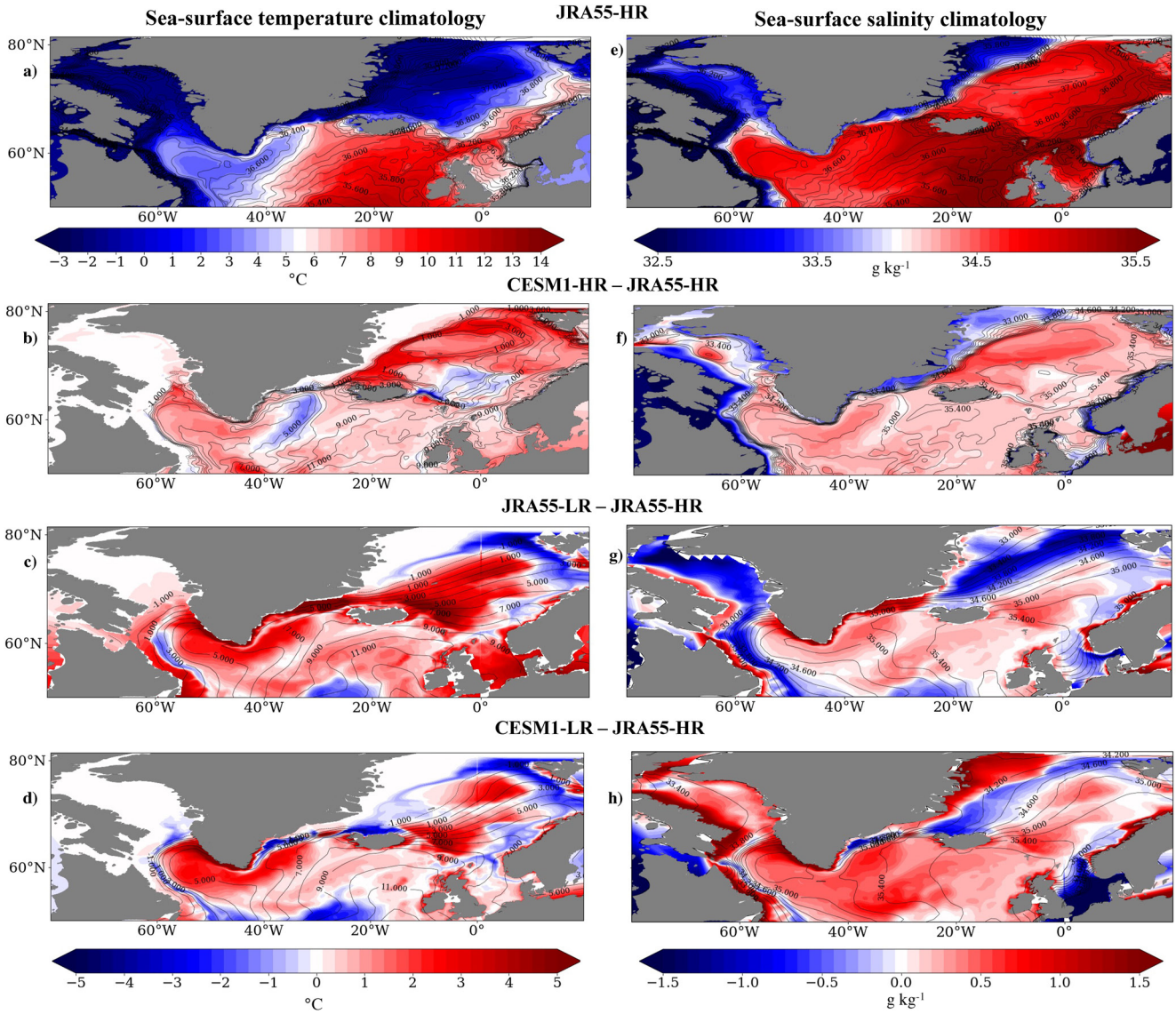

Figure 8. (a) JRA55-HR sea-surface potential temperature climatology. (b–d) Sea-surface potential temperature climatologies (contours) and anomalies relative to JRA55-HR (colors) for (b) CESM1-HR, (c) JRA55-LR, and (d) CESM1-LR. (e) JRA55-HR sea-surface salinity climatology. (f–h) Sea-surface salinity climatologies (contours) and anomalies relative to JRA55-HR (colors) for (f) CESM1-HR, (g) JRA55-LR, and (h) CESM1-LR.

fields in the Labrador Sea explain the narrower WMT peaks in the LR simulations compared to JRA55-HR and CESM1-HR. Also, the high densities in the GIN Seas in CESM1-HR explain why there is positive WMT in that region at higher densities than what is seen in the other models (Figure 3c).

CESM1-HR best reproduces the surface heat fluxes found in JRA55-HR (Figures 7e and 7f), with some positive anomalies in the central and northern Labrador Sea and broad negative anomalies throughout the IIB and GIN Seas, aside from the far north, which exhibits positive anomalies (Figure 7f). The larger (more negative) heat fluxes in the IIB and GIN Seas explain the larger IIB and GIN WMT in CESM1-HR compared to JRA55-HR, given that stronger heat fluxes drive higher WMT. JRA55-LR exhibits larger positive anomalies in the Labrador Sea and northern GIN Seas compared to CESM1-HR (Figure 7g). In CESM1-LR, there is a mix of positive and negative anomalies in the Labrador Sea, and larger negative anomalies in the central GIN Seas (Figure 7h).

Surprisingly, CESM1-HR reproduces the WMT, sea-surface heat fluxes, SSTs, and salinities of JRA55-HR far better than JRA55-LR does, which highlights the importance of ocean resolution in accurately representing these

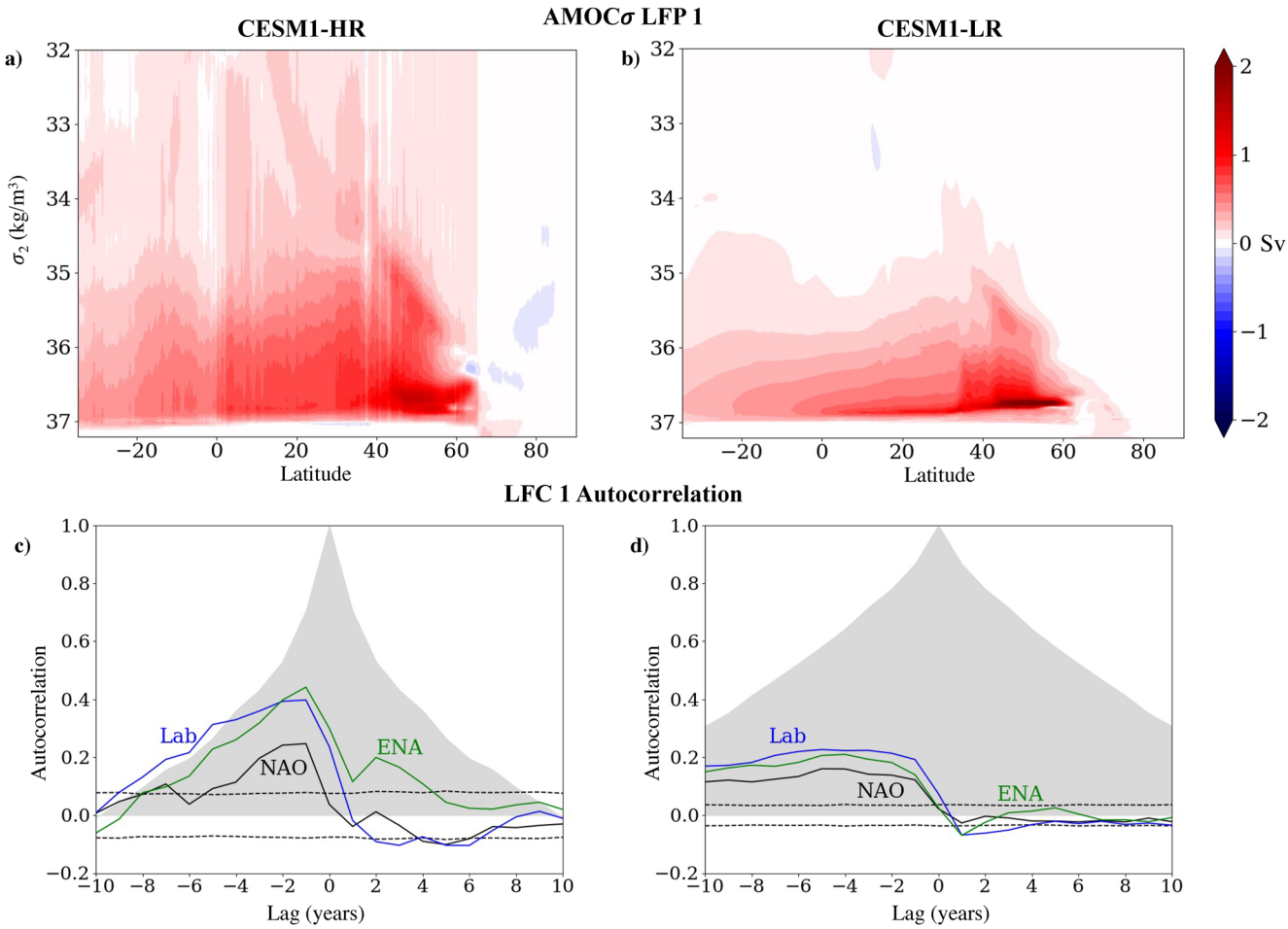

Figure 9. Top row: Low-frequency pattern (LFP) 1 of AMOC for (a) CESM1-HR and (b) CESM1-LR. Bottom row: Autocorrelations of low-frequency component (LFC) 1 (shaded), correlation of the North Atlantic Oscillation (NAO) with LFC 1 (solid black lines) and significance levels (dashed black lines), and correlations of both the Labrador Sea (blue lines) and Eastern North Atlantic (ENA; green lines) winter mixed-layer depths with LFC 1 for (c) CESM1-HR and (d) CESM1-LR. NAO here is defined as the difference between the sea-level pressure between the Azores (25.5°W, 37.5°N) and Iceland (21.5°W, 64.5°N). The ENA here includes both the IIB and the GIN Seas.

variables. It also indicates that simply forcing an ocean model with atmospheric reanalyses is insufficient if the ocean is low resolution.

4. Mechanisms of Low-Frequency AMOC Variability in High- and Low-Resolution Versions of CESM

We next turn our attention to the mechanisms driving low-frequency AMOC variability. We apply a LFCA (R. C. Wills et al., 2018; R. C. J. Wills et al., 2019) to AMOC in density coordinates in CESM1-HR and CESM1-LR's preindustrial control simulations. The purpose of using LFCA is to create an index that emphasizes low-frequency variability in the overturning stream function data without losing any time resolution due to low-pass filtering, allowing us to more easily determine lead–lag relationships.

We focus on the first low-frequency pattern (LFP) of AMOC, which is the linear combination of the leading empirical orthogonal functions (EOFs) with the highest ratio of low-frequency variance to total variance in its corresponding timeseries (i.e., its low-frequency component; LFC). The LFP (Figure 9) represents the AMOC anomaly associated with a one standard deviation (1σ) anomaly in the corresponding LFC. Here, low-frequency variance is defined as the variance at 10-year and longer time scales, computed using a Lanczos filter with a low-pass cutoff of 10 years. Low-pass filtering is only used to identify the LFP, and all information about

high-frequency variations is preserved. For both models, we include the six leading EOFs in the LFCA. The choice of the number of EOFs does not substantially influence the results for either model.

In our previous analysis of low-resolution-coupled model simulations (Oldenburg et al., 2021), we found that WMT in the Labrador Sea plays a more substantial role in driving AMOC and OHT variability than would be expected based on its role in driving the climatology of AMOC and OHT. Here, we examine whether the model resolution affects this result, given that higher-resolution models represent Labrador Sea processes much better than low-resolution ones (see Section 3). Hence, here we carry out an analysis similar to Oldenburg et al. (2021) with a focus entirely on AMOC instead of Atlantic OHT. Our goal is to determine whether the mechanisms of low-frequency AMOC variability in low-resolution simulations still hold in high-resolution models. We first compute the LFPs and LFCs of annual-mean AMOC in CESM1-HR and CESM1-LR, then calculate lead–lag regressions between the first LFC and other fields, including winter mixed-layer depth, surface-forced WMT, winter SLP, and AMOC. Although the LFPs already give the AMOC anomaly at lag 0, the pattern of AMOC anomalies evolves over time and therefore can look different at lead and lag times (Figure S3 in Supporting Information S1).

The first LFPs of AMOC in CESM1-HR and CESM1-LR share some common features, with maxima in the midlatitudes to subpolar latitudes. In CESM1-LR, the maximum value is equal to 2.51 Sv and is located at 53.5°N and $\sigma_2 = 36.74$ kg m^{-3}, which is substantially stronger and at a higher latitude and density than in CESM1-HR, where the maximum value is equal to 1.48 Sv and is located at 47°N and $\sigma_2 = 36.675$ kg m^{-3}. The AMOC peak is also more localized than in CESM1-HR. The other major difference is that the positive values extend to lower densities in CESM1-HR compared to CESM1-LR. The ratios of low frequency to total variance for the LFCs are equal to 0.70 and 0.87 for CESM1-HR and CESM1-LR, respectively, and the LFC autocorrelations remain high for much longer lag times in CESM1-LR compared to CESM1-HR (Figures 9c and 9d). In CESM1-HR, the autocorrelation drops off more quickly, reaching zero by lag 10 years (Figure 9c). The lower ratio of low frequency to total variance in CESM1-HR indicates that that model's LFC includes more high-frequency variability, and the lower autocorrelation is consistent with an AMOC that changes more rapidly over lead and lag times (Figure S3 in Supporting Information S1).

In CESM1-HR, there is a persistent SLP pattern linked to anomalous northwesterly winds off eastern North America starting at about lead 4 years (Figure 10b). This SLP pattern remains until lag 0, which is the time of maximum AMOC (Figures 10a–10d). This pattern's persistence must result from processes in the ocean, because the persistence time scale of atmospheric anomalies is less than a month (Ambaum & Hoskins, 2002). At lag 0, the SLP pattern becomes more zonal and the eastern SLP anomaly intensifies (Figure 10d). After lag 0, the pattern reverses (Figures 10e and 10f) with a pattern that looks similar to the negative phase of the NAO. In CESM1-LR, there is a similar SLP pattern at lead times and at lag 0 (Figures 10g–10j). After lag 0, the SLP pattern dissipates completely in CESM1-LR (Figure 10l). However, unlike many low-resolution models, including CESM1-LR and the LR models discussed in Oldenburg et al. (2021), CESM1-HR shows a coherent SLP pattern after the time of maximum AMOC. This indicates an atmospheric response to the low-frequency AMOC variability not seen in the equivalent low-resolution model, but which has been reported in a number of observational studies (Czaja & Frankignoul, 1999, 2002; Czaja et al., 2019; Gastineau & Frankignoul, 2015; Venzke et al., 1999; S. M. Wills et al., 2016). This response can also be seen in the negative lagged correlation of the NAO with LFC 1 (Figure 9c), which peaks at a lag of 5 years.

In both HR and LR models, the effect of the SLP pattern at lead times on the subpolar winter mixed-layer depths can be seen in Figure S4 in Supporting Information S1, which shows deepening mixed-layer depths, particularly in the Labrador Sea. The time evolution of Labrador Sea mixed-layer depth mirrors that of the NAO (Figures 9c and 9d). The Eastern North Atlantic (ENA) mixed-layer depth does follow the NAO to some degree, especially in CESM1-LR, but it does not mirror it to the same degree as the Labrador Sea in CESM1-HR (Figures 9c and 9d).

In CESM1-HR, WMT in the Labrador Sea strengthens in the years leading up to maximum AMOC, reaching its maximum at lead 2, concurrent with the strengthening of AMOC and the mixed layer deepening in the Labrador Sea, IIB, and GIN Seas (Figure 11a). This peak is equal to 1.29 Sv and is located at $\sigma_2 = 36.83$ kg m^{-3}, which is at a substantially higher density than the location of the maximum AMOC anomaly at lag 0, but is still within the density range of the broad positive AMOC anomaly. After lead 2, the WMT rapidly decreases. The ENA WMT, which includes both the GIN Seas and IIB, also increases at lead times, peaking at lead 1 (not shown). This peak

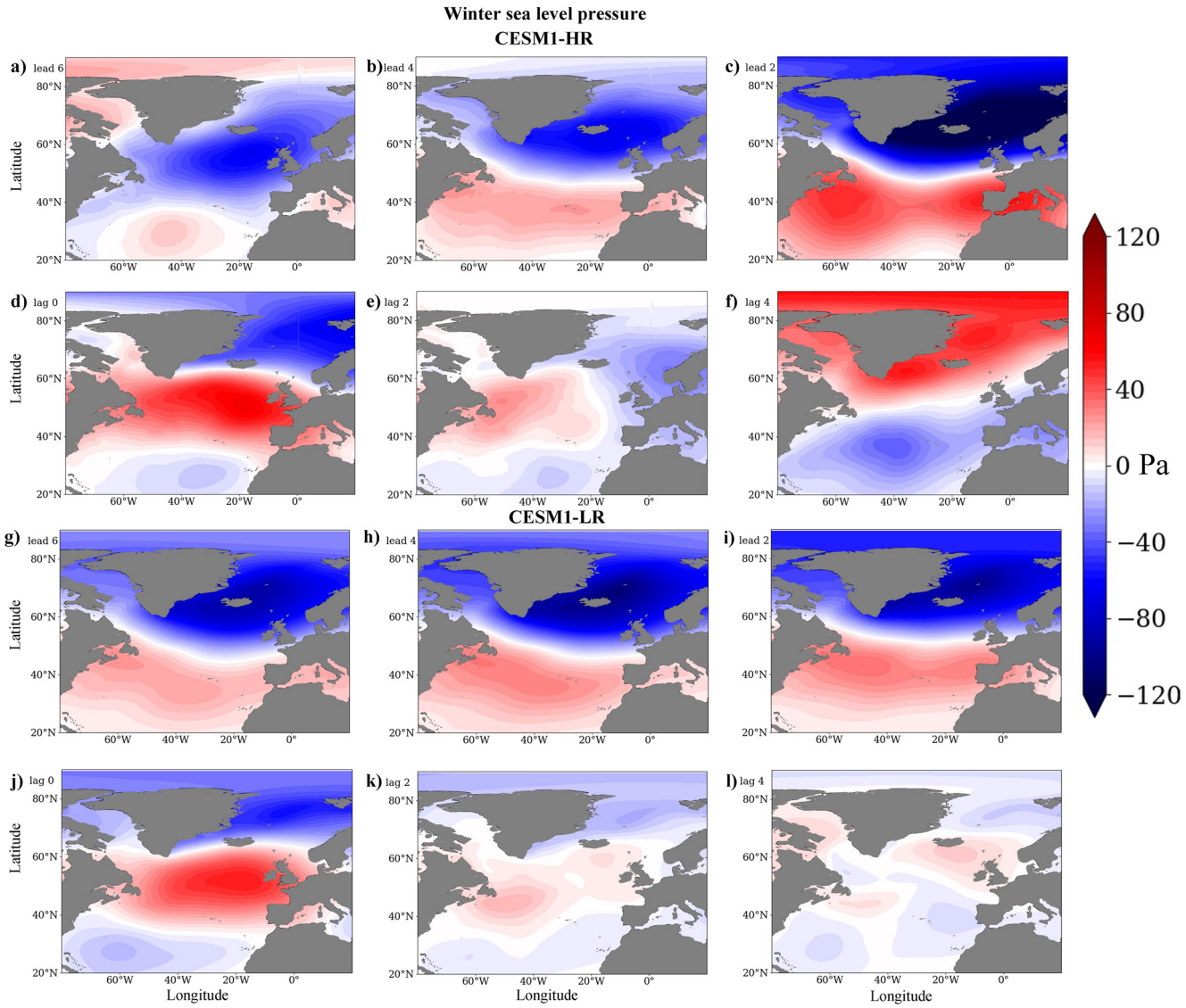

Figure 10. Lead–lag regressions of sea-level pressure averaged over January–March onto the first LFC of AMOC for (a–f) CESM1-HR and (g–l) CESM1-LR. Lead times represent anomalies that lead the LFC, that is, before the time of maximum AMOC. Because the LFCs are unitless, the units of the regressions are Pa (N/m^2).

is equal to 0.83 Sv and is located at $\sigma_2 = 36.84$, which is further from the peak in AMOC than the Labrador Sea WMT peak. The peak in ENA WMT is mostly due to changes in IIB WMT rather than the GIN Seas (not shown).

In CESM1-LR, the Labrador Sea WMT also increases at lead times, reaching its maximum at lead 2 years (Figure 11b). This maximum is equal to 3.99 Sv and is located at $\sigma_2 = 36.76$ kg m^{-3}, which is at a slightly higher density than the maximum AMOC anomaly. The ENA WMT also strengthens at lead times but already peaks by lead 4 years (Figure 11d). This peak is equal to 0.82 Sv and is located at $\sigma_2 = 36.62$ kg m^{-3}, which is at a substantially lower density than the maximum AMOC anomaly. This WMT increase is mostly due to changes in the IIB rather than the GIN Seas (not shown).

Based on these results, the mechanisms of AMOC variability between CESM1-HR and CESM1-LR are qualitatively similar but still have quantitative differences. In both models, the Labrador Sea plays a dominant role in driving low-frequency AMOC variability, and the leading SLP patterns are similar. The primary differences are that CESM1-HR, unlike CESM1-LR, shows a substantial atmospheric response after the time of maximum AMOC and that the Labrador Sea does not dominate the WMT variability as much as it does in CESM1-LR.

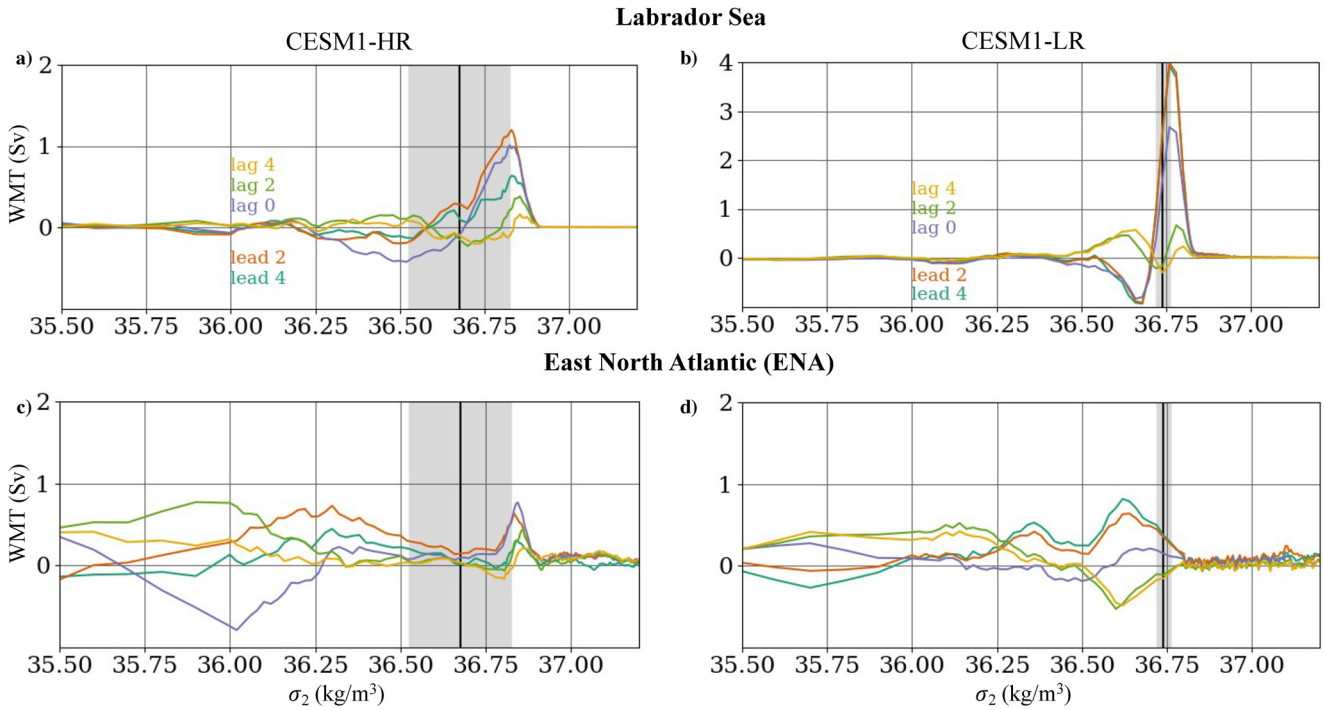

Figure 11. Lead–lag regressions of water mass transformation (WMT) onto the first LFC of AMOC for CESM1-HR (left column) and CESM1-LR (right column). (a, b) WMT integrated throughout the Labrador Sea section. (c, d) WMT integrated throughout the Eastern North Atlantic (ENA) region. The black vertical lines represent the density where the AMOC regression at lag 0 is at its maximum in each model. The gray shaded areas show the density range where the AMOC regression at lag 0 is within 25% of its maximum value. The black lines in Figure 1 show what we consider to be the Labrador Sea, the IIB, and the GIN Seas in this calculation. The ENA here includes both the GIN Seas and the IIB. Lead times represent anomalies that lead the LFC, that is, before the time of maximum AMOC. Because the LFCs are unitless, the units of the regressions are Sv. Note the difference in scale between (b) and the others.

5. Discussion and Conclusions

In Section 3, we showed that a coupled model with increased atmospheric and ocean resolutions accurately reproduces the WMT, SSTs, and sea-surface salinities found in a reanalysis-forced high-resolution ocean simulation. The ocean resolution appears to be particularly important, as even a low-resolution ocean simulation forced with atmospheric reanalysis data does not represent the WMT as accurately as the high-resolution-coupled model simulation. This illustrates the importance of resolving, rather than parameterizing, mesoscale eddies for the ability to accurately represent mixed-layer depth and deep water formation, particularly in the Labrador Sea.

The better representation of WMT is explained by a more accurate representation of the density structure in the high-resolution simulation compared to the low-resolution simulations, which have relatively uniform density fields in comparison, particularly in the Labrador Sea. Smaller discrepancies in surface heat fluxes in the deep water formation regions in the high-resolution simulation also help explain why it captures the climatological WMT better than the low-resolution simulations.

In Section 4, we used LFCA to assess the mechanisms of low-frequency AMOC variability in high- and low-resolution versions of the same model, finding that the mechanisms are qualitatively similar but quantitatively different. The Labrador Sea WMT still plays a major role in the WMT and AMOC variability in the high-resolution model despite the fact that it shows a smaller role for the Labrador Sea in climatological WMT and AMOC than the low-resolution version. The analysis here neglects interior ocean mixing. However, despite the fact that most of the Labrador Sea WMT changes occur at higher densities than the AMOC changes, the Labrador Sea's dominance in AMOC variability likely still holds because mixing tends to make the densest water lighter. This corroborates the results found in recent studies of low- and high-resolution-coupled models (Oldenburg et al., 2021; Yeager et al., 2021).

One noteworthy difference between the high- and low-resolution simulations is that the high-resolution simulation shows a substantial atmospheric response to the AMOC variability not seen in the low-resolution simulation.

This type of atmospheric response has been seen in a study of a medium-resolution-coupled model, but with a longer lag time between the AMOC change and the negative NAO response (Wen et al., 2016). NAO-like responses of differing signs to AMOC variability have also been found in other modeling studies (Dong & Sutton, 2003; Frankignoul et al., 2013, 2015; Gastineau & Frankignoul, 2012; Gastineau et al., 2013). The model simulations we analyzed here do not give insight into whether the atmospheric or oceanic resolution is responsible for the increased atmospheric response to AMOC variability in CESM1-HR, but recent work suggests that the atmospheric response to near-surface ocean anomalies is larger at higher atmospheric resolution (e.g., Czaja et al., 2019). As mentioned above, atmospheric responses to North Atlantic Ocean variability have also been found in observational studies, primarily via analyses of SST variations, albeit typically with much shorter lag times between the peak in the SST patterns and the SLP response (Czaja & Frankignoul, 1999, 2002; Gastineau & Frankignoul, 2015; Venzke et al., 1999; S. M. Wills et al., 2016). Overall, it appears that the mode of AMOC variability in the high-resolution model is associated with stronger anomalies in atmospheric fields (i.e., SLP), while the low-resolution version is associated with stronger anomalies in ocean fields, namely WMT, particularly in the Labrador Sea.

Our results suggest that increasing the ocean and atmospheric resolution of a coupled model substantially improves the representation of climatological AMOC and WMT. However, the mechanisms driving low-frequency AMOC variability remain qualitatively similar even though the climatologies differ. The mechanisms of low-frequency variability are consistent with what was found in three low-resolution-coupled models with distinct representations of WMT in the different subpolar North Atlantic deep water formation regions, which all showed similar mechanisms of AMOC and OHT variability, with the Labrador Sea playing a dominant role (Oldenburg et al., 2021).

Data Availability Statement

CESM1-LR data can be downloaded at https://earthsystemgrid.org. CESM1-HR data can be found at https://ihesp.tamu.edu/. Postprocessed data used to create some of the figures in this paper can be found at https://faculty.washington.edu/karmour/code/Oldenburg/. Further JRA55-LR and JRA55-HR data used in this study are available on request. MATLAB and Python code for LFCA is available at https://github.com/rcjwills/lfca.

Acknowledgments
The authors are grateful for support from the National Science Foundation through grants OCE-1523641 and OCE-1850900 (D. O. and K. C. A.), and AGS-1929775 and AGS-2128409 (R. C. J. W.). L. T. acknowledges support from NASA grants NNX17AH56G and 80NSSC20K0787. We thank NCAR and iHESP for making their model output available.

References

Ambaum, M. H. P., & Hoskins, B. J. (2002). The NAO troposphere–stratosphere connection. *Journal of Climate*, *15*(14), 1969–1978. https://doi.org/10.1175/1520-0442(2002)015<1969:TNTSC>2.0.CO;2

Bailey, D. A., Rhines, P. B., & Häkkinen, S. (2005). Formation and pathways of North Atlantic Deep Water in a coupled ice–ocean model of the Arctic–North Atlantic Oceans. *Climate Dynamics*, *25*(5), 497–516. https://doi.org/10.1007/s00382-005-0050-3

Brambilla, E., & Talley, L. D. (2008). Subpolar Mode Water in the northeastern Atlantic: 1. Averaged properties and mean circulation. *Journal of Geophysical Research*, *113*, C04025. https://doi.org/10.1029/2006JC004062

Chang, P., Zhang, S., Danabasoglu, G., Yeager, S. G., Fu, H., Wang, H., et al. (2020). An unprecedented set of high-resolution Earth system simulations for understanding multiscale interactions in climate variability and change. *Journal of Advances in Modeling Earth Systems*, *12*, e2020MS002298. https://doi.org/10.1029/2020MS002298

Chassignet, E. P., Yeager, S. G., Fox-Kemper, B., Bozec, A., Castruccio, F., Danabasoglu, G., et al. (2020). Impact of horizontal resolution on global ocean–sea ice model simulations based on the experimental protocols of the Ocean Model Intercomparison Project phase 2 (OMIP-2). *Geoscientific Model Development*, *13*(9), 4595–4637. https://doi.org/10.5194/gmd-13-4595-2020

Covey, C., & Thompson, S. L. (1989). Testing the effects of ocean heat transport on climate. *Global and Planetary Change*, *1*(4), 331–341. https://doi.org/10.1016/0921-8181(89)90009-X

Czaja, A., & Frankignoul, C. (1999). Influence of the North Atlantic SST on the atmospheric circulation. *Geophysical Research Letters*, *26*(19), 2969–2972. https://doi.org/10.1029/1999GL900613

Czaja, A., & Frankignoul, C. (2002). Observed impact of Atlantic SST anomalies on the North Atlantic Oscillation. *Journal of Climate*, *15*(6), 606–623. https://doi.org/10.1175/1520-0442(2002)015<0606:OIOASA>2.0.CO;2

Czaja, A., Frankignoul, C., Minobe, S., & Vannière, B. (2019). Simulating the midlatitude atmospheric circulation: What might we gain from high-resolution modeling of air–sea interactions? *Current Climate Change Reports*, *5*(4), 390–406. https://doi.org/10.1007/s40641-019-00148-5

Day, J. J., Hargreaves, J. C., Annan, J. D., & Abe-Ouchi, A. (2012). Sources of multi-decadal variability in Arctic sea ice extent. *Environmental Research Letters*, *7*(3), 034011. https://doi.org/10.1088/1748-9326/7/3/034011

Delworth, T. L., & Zeng, F. (2016). The impact of the North Atlantic Oscillation on climate through its influence on the Atlantic Meridional Overturning Circulation. *Journal of Climate*, *29*(3), 941–962. https://doi.org/10.1175/JCLI-D-15-0396.1

Delworth, T. L., Zeng, F., Vecchi, G. A., Yang, X., Zhang, L., & Zhang, R. (2016). The North Atlantic Oscillation as a driver of rapid climate change in the Northern Hemisphere. *Nature Geoscience*, *9*(7), 509–512. https://doi.org/10.1038/ngeo2738

Dong, B., & Sutton, R. T. (2003). Variability of Atlantic Ocean heat transport and its effects on the atmosphere. *Annals of Geophysics*, *46*(1). https://doi.org/10.4401/ag-3391

Eden, C., & Jung, T. (2001). North Atlantic interdecadal variability: Oceanic response to the North Atlantic Oscillation (1865–1997). *Journal of Climate*, *14*(5), 676–691. https://doi.org/10.1175/1520-0442(2001)014<0676:NAIVOR>2.0.CO;2

Frankignoul, C., Gastineau, G., & Kwon, Y.-O. (2013). The influence of the AMOC variability on the atmosphere in CCSM3. *Journal of Climate*, *26*(24), 9774–9790. https://doi.org/10.1175/JCLI-D-12-00862.1

Frankignoul, C., Gastineau, G., & Kwon, Y.-O. (2015). Wintertime atmospheric response to North Atlantic ocean circulation variability in a climate model. *Journal of Climate*, *28*(19), 7659–7677. https://doi.org/10.1175/JCLI-D-15-0007.1

Garcia-Quintana, Y., Courtois, P., Hu, X., Pennelly, C., Kieke, D., & Myers, P. G. (2019). Sensitivity of Labrador Sea water formation to changes in model resolution, atmospheric forcing, and freshwater input. *Journal of Geophysical Research: Oceans*, *124*, 2126–2152. https://doi.org/10.1029/2018JC014459

Gastineau, G., D'Andrea, F., & Frankignoul, C. (2013). Atmospheric response to the North Atlantic ocean variability on seasonal to decadal time scales. *Climate Dynamics*, *40*(9), 2311–2330. https://doi.org/10.1007/s00382-012-1333-0

Gastineau, G., & Frankignoul, C. (2012). Cold-season atmospheric response to the natural variability of the Atlantic Meridional Overturning Circulation. *Climate Dynamics*, *39*(1), 37–57. https://doi.org/10.1007/s00382-011-1109-y

Gastineau, G., & Frankignoul, C. (2015). Influence of the North Atlantic SST variability on the atmospheric circulation during the twentieth century. *Journal of Climate*, *28*(4), 1396–1416. https://doi.org/10.1175/JCLI-D-14-00424.1

Grist, J. P., Marsh, R., & Josey, S. A. (2009). On the relationship between the North Atlantic Meridional Overturning Circulation and the surface-forced overturning streamfunction. *Journal of Climate*, *22*(19), 4989–5002. https://doi.org/10.1175/2009JCLI2574.1

Harada, Y., Kamahori, H., Kobayashi, C., Endo, H., Kobayashi, S., Ota, Y., et al. (2016). The JRA-55 reanalysis: Representation of atmospheric circulation and climate variability. *Meteorological Magazine. No. 2*, *94*(3), 269–302. https://doi.org/10.2151/jmsj.2016-015

Heuze, C. (2017). North Atlantic deep water formation and AMOC in CMIP5 models. *Ocean Science*, *13*(4), 609–622. https://doi.org/10.5194/os-13-609-2017

Hurrell, J. W. (2013). The Community Earth System Model: A framework for collaborative research. *Bulletin of the American Meteorological Society*, *94*, 1339–1360. https://doi.org/10.1175/bams-d-12-00121.1

Isachsen, P. E., Mauritzen, C., & Svendsen, H. (2007). Dense water formation in the Nordic Seas diagnosed from sea surface buoyancy fluxes. *Deep Sea Research Part I: Oceanographic Research Papers*, *54*(1), 22–41. https://doi.org/10.1016/j.dsr.2006.09.008

Josey, S. A., Grist, J. P., & Marsh, R. (2009). Estimates of Meridional Overturning Circulation variability in the North Atlantic from surface density flux fields. *Journal of Geophysical Research*, *114*, C09022. https://doi.org/10.1029/2008JC005230

Kim, W. M., Yeager, S., Chang, P., & Danabasoglu, G. (2018). Low-frequency North Atlantic climate variability in the Community Earth System Model large ensemble. *Journal of Climate*, *31*(2), 787–813. https://doi.org/10.1175/JCLI-D-17-0193.1

Kim, W. M., Yeager, S., & Danabasoglu, G. (2020). Atlantic multidecadal variability and associated climate impacts initiated by ocean thermohaline dynamics. *Journal of Climate*, *33*(4), 1317–1334. https://doi.org/10.1175/JCLI-D-19-0530.1

Kim, W. M., Yeager, S., & Danabasoglu, G. (2021). Revisiting the causal connection between the great salinity anomaly of the 1970s and the shutdown of Labrador Sea deep convection. *Journal of Climate*, *34*(2), 675–696. https://doi.org/10.1175/JCLI-D-20-0327.1

Kobayashi, S., Ota, Y., Harada, Y., Ebita, A., Moriya, M., Onoda, H., et al. (2015). The JRA-55 reanalysis: General specifications and basic characteristics. *The Meteorological Magazine, No. 2*, *93*(1), 5–48. https://doi.org/10.2151/jmsj.2015-001

Kwon, Y.-O., & Frankignoul, C. (2014). Mechanisms of multidecadal Atlantic Meridional Overturning Circulation variability diagnosed in depth versus density space. *Journal of Climate*, *27*(24), 9359–9376. https://doi.org/10.1175/JCLI-D-14-00228.1

Langehaug, H. R., Medhaug, I., Eldevik, T., & Otterå, O. H. (2012). Arctic/Atlantic exchanges via the subpolar gyre. *Journal of Climate*, *25*(7), 2421–2439. https://doi.org/10.1175/JCLI-D-11-00085.1

Langehaug, H. R., Rhines, P. B., Eldevik, T., Mignot, J., & Lohmann, K. (2012). Water mass transformation and the North Atlantic Current in three multicentury climate model simulations. *Journal of Geophysical Research*, *117*, C11001. https://doi.org/10.1029/2012JC008021

Locarnini, R. A., Mishonov, A. V., Antonov, J. I., Boyer, T. P., Garcia, H. E., Baranova, O. K., et al. (2013). *Temperature. Vol. 1, World Ocean Atlas 2013*. *NOAA Atlas NESDIS 73*.

MacMartin, D. G., Zanna, L., & Tziperman, E. (2016). Suppression of Atlantic Meridional Overturning Circulation variability at increased CO_2. *Journal of Climate*, *29*(11), 4155–4164. https://doi.org/10.1175/JCLI-D-15-0533.1

Marsh, R. (2000). Recent variability of the North Atlantic thermohaline circulation inferred from surface heat and freshwater fluxes. *Journal of Climate*, *13*(18), 3239–3260. https://doi.org/10.1175/1520-0442(2000)013<3239:RVOTNA>2.0.CO;2

McCartney, M. S., & Talley, L. D. (1982). The Subpolar Mode Water of the North Atlantic Ocean. *Journal of Physical Oceanography*, *12*(11), 1169–1188. https://doi.org/10.1175/1520-0485(1982)012<1169:TSMWOT>2.0.CO;2

Mecking, J. V., Keenlyside, N. S., & Greatbatch, R. J. (2015). Multiple timescales of stochastically forced North Atlantic Ocean variability: A model study. *Ocean Dynamics*, *65*(9), 1367–1381. https://doi.org/10.1007/s10236-015-0868-0

Menary, M. B., Hodson, D. L. R., Robson, J. I., Sutton, R. T., Wood, R. A., & Hunt, J. A. (2015). Exploring the impact of CMIP5 model biases on the simulation of North Atlantic decadal variability. *Geophysical Research Letters*, *42*, 5926–5934. https://doi.org/10.1002/2015GL064360

Newsom, E. R., Bitz, C. M., Bryan, F. O., Abernathey, R., & Gent, P. R. (2016). Southern ocean deep circulation and heat uptake in a high-resolution climate model. *Journal of Climate*, *29*(7), 2597–2619. https://doi.org/10.1175/JCLI-D-15-0513.1

Oldenburg, D., Armour, K. C., Thompson, L., & Bitz, C. M. (2018). Distinct mechanisms of ocean heat transport into the Arctic under internal variability and climate change. *Geophysical Research Letters*, *45*, 7692–7700. https://doi.org/10.1029/2018GL078719

Oldenburg, D., Wills, R. C. J., Armour, K. C., Thompson, L., & Jackson, L. C. (2021). Mechanisms of low-frequency variability in North Atlantic Ocean heat transport and AMOC. *Journal of Climate*, *34*(12), 4733–4755. https://doi.org/10.1175/JCLI-D-20-0614.1

Pérez-Brunius, P., Rossby, T., & Watts, D. R. (2004). Transformation of the warm waters of the North Atlantic from a geostrophic streamfunction perspective. *Journal of Physical Oceanography*, *34*(10), 2238–2256. https://doi.org/10.1175/1520-0485(2004)034<2238:TOTWWO>2.0.CO;2

Pickart, R. S., & Spall, M. A. (2007). Impact of Labrador Sea convection on the North Atlantic Meridional Overturning Circulation. *Journal of Physical Oceanography*, *37*(9), 2207–2227. https://doi.org/10.1175/JPO3178.1

Roberts, C. D., Waters, J., Peterson, K. A., Palmer, M. D., McCarthy, G. D., Frajka-Williams, E., et al. (2013). Atmosphere drives recent interannual variability of the Atlantic Meridional Overturning Circulation at 26.5°N. *Geophysical Research Letters*, *40*, 5164–5170. https://doi.org/10.1002/grl.50930

Robson, J., Ortega, P., & Sutton, R. (2016). A reversal of climatic trends in the North Atlantic since 2005. *Nature Geoscience*, *9*(7), 513–517. https://doi.org/10.1038/ngeo2727

Sein, D. V., Koldunov, N. V., Danilov, S., Sidorenko, D., Wekerle, C., Cabos, W., et al. (2018). The relative influence of atmospheric and oceanic model resolution on the circulation of the North Atlantic Ocean in a coupled climate model. *Journal of Advances in Modeling Earth Systems*, *10*, 2026–2041. https://doi.org/10.1029/2018MS001327

Straneo, F. (2006). On the connection between dense water formation, overturning, and poleward heat transport in a convective basin. *Journal of Physical Oceanography*, *36*(9), 1822–1840. https://doi.org/10.1175/JPO2932.1

Treguier, A. M., Theetten, S., Chassignet, E. P., Penduff, T., Smith, R., Talley, L., et al. (2005). The North Atlantic subpolar gyre in four high-resolution models. *Journal of Physical Oceanography*, *35*(5), 757–774. https://doi.org/10.1175/JPO2720.1

Venzke, S., Allen, M. R., Sutton, R. T., & Rowell, D. P. (1999). The atmospheric response over the North Atlantic to decadal changes in sea surface temperature. *Journal of Climate*, *12*(8), 2562–2584. https://doi.org/10.1175/1520-0442(1999)012<2562:TAROTN>2.0.CO;2

Wen, N., Frankignoul, C., & Gastineau, G. (2016). Active AMOC-NAO coupling in the IPSL-CM5A-MR climate model. *Climate Dynamics*, *47*(7), 2105–2119. https://doi.org/10.1007/s00382-015-2953-y

Wills, R. C., Schneider, T., Wallace, J. M., Battisti, D. S., & Hartmann, D. L. (2018). Disentangling global warming, multidecadal variability, and El Niño in Pacific temperatures. *Geophysical Research Letters*, *45*, 2487–2496. https://doi.org/10.1002/2017GL076327

Wills, R. C. J., Armour, K. C., Battisti, D. S., & Hartmann, D. L. (2019). Ocean–atmosphere dynamical coupling fundamental to the Atlantic multidecadal oscillation. *Journal of Climate*, *32*(1), 251–272. https://doi.org/10.1175/JCLI-D-18-0269.1

Wills, S. M., Thompson, D. W. J., & Ciasto, L. M. (2016). On the observed relationships between variability in gulf stream sea surface temperatures and the atmospheric circulation over the North Atlantic. *Journal of Climate*, *29*(10), 3719–3730. https://doi.org/10.1175/JCLI-D-15-0820.1

Winton, M., Anderson, W. G., Delworth, T. L., Griffies, S. M., Hurlin, W. J., & Hurlin, A. (2014). Has coarse ocean resolution biased simulations of transient climate sensitivity? *Geophysical Research Letters*, *41*, 8522–8529. https://doi.org/10.1002/2014GL061523

Yeager, S., Castruccio, F., Chang, P., Danabasoglu, G., Maroon, E., Small, J., et al. (2021). An outsized role for the Labrador Sea in the multidecadal variability of the Atlantic overturning circulation. *Science Advances*, *7*(41), eabh3592. https://doi.org/10.1126/sciadv.abh3592

Zhang, R. (2015). Mechanisms for low-frequency variability of summer Arctic sea ice extent. *Proceedings of the National Academy of Sciences of the United States of America*, *112*(15), 4570–4575. https://doi.org/10.1073/pnas.1422296112

Zweng, M. M., Reagan, J. R., Antonov, J. I., Locarnini, R. A., Mishonov, A. V., Timothy, P., et al. (2013). *Salinity. Vol. 2, World Ocean Atlas 2013. NOAA Atlas NESDIS, 74, 39*.